
Leiden University

# Polarization and angle dependence of transmission through subwavelength hole arrays

Bachelor Project

July 11, 2013

*Author:*
Kim Vendel

*Supervisors:*
Martin van Exter
Flavio Mariani
Christoph Keller
Frans Snik

# Contents

**Introduction** **1**

**1 Theory** **2**
1.1 Surface Plasmon Polaritons . . . 2
1.2 Dipole radiation . . . 3
1.3 Extraordinary optical transmission and hole arrays . . . 4
1.4 Diffraction orders . . . 6
1.5 Theory for this project . . . 7

**2 Materials and methods** **9**
2.1 Sample . . . 9
2.2 Experimental setup . . . 10
2.3 Data acquisition . . . 13
2.4 Analysis of the data . . . 13

**3 Experiments zeroth order transmission** **15**
3.1 Results and fitting of the two measurements . . . 15
3.2 Discussion . . . 17

**4 Experiments pp configuration** **18**
4.1 Results . . . 18
4.2 Analysis . . . 21
4.3 Discussion . . . 24

**5 Experiments ss configuration** **25**
5.1 Results . . . 25
5.2 Analysis . . . 27
5.3 Discussion . . . 29

**6 Experiments with illumination on the chromium side** **31**
6.1 Results pp configuration . . . 31
6.2 Analysis pp configuration . . . 33
6.3 Results ss configuration . . . 34
6.4 Analysis ss configuration . . . 35
6.5 Discussion . . . 36

**7 Astronomical relevance** **38**

**8 Conclusions** **40**

**Bibliography** **42**

# Introduction

This thesis presents a study of transmission in the diffraction orders through a sample consisting of a gold film perforated with rectangular arrays of subwavelength holes on a glass substrate.
Already in 1944 Bethe wrote about the diffraction of electromagnetic waves by subwavelength holes [1], showing a full theoretical description of this phenomenon. But in 1998 Ebbesen discovered that more light passes through a metal film perforated with multiple subwavelength holes than expected from Bethe's theory [2]. He called this effect the extraordinary optical transmission (EOT) and found out it was caused by the coupling of light to surface plasmon polaritons (SPPs). SPPs are surface waves of electronic oscillations on a metal-dielectric interface and were already known in 1957 when Ritchie first published about them [3].

Since the discovery in 1998 a lot of research has been done on the EOT and the contributing processes. The transmission of light through subwavelength structures can in first approximation be described in terms of electric and magnetic dipoles [4]. Liu and Lalanne elaborated a microscopic model to describe the transmission [5] in terms of direct transmission through the holes and the contribution of coupling to SPPs. Van Beijnum showed in 2012 that this theory gives very accurate fits to the zeroth order transmission spectra [6].

For this project we focused on experiments in the diffraction orders of our sample to find the angle and polarization dependence of the transmission. The goal was to learn more about the strength and orientation of the different dipoles that describe the transmission. To achieve that goal we measured the intensity in diffraction orders for several arrays of holes with a different hole spacing. This was performed with two different polarizations.
To find the dipole contributions of both the direct transmission and SPPs we used the model of Liu and Lalanne to fit the spectra and separate these two contributions.

This thesis starts with the theory applied to the project in chapter 1 to explain SPPs, dipoles, EOT and diffraction orders. Next, chapter 2 describes the sample, experimental setup and fitting procedures. As a first experiment, we compared the zeroth order transmission with earlier experiments on the same sample, which can be found in chapter 3. Thereafter, experiments have been performed on two sides of the sample with two different polarizations. Results, analysis and discussion of these experiments are in chapter 4 to chapter 6. Also the astronomical relevance of this project will be discussed in chapter 7. Finally we draw conclusions in chapter 8.

# Chapter 1

# Theory

This section contains the theory of the processes relevant for our research on the gold-dielectric sample with arrays of subwavelength holes. Surface plasmon polaritons and their contribution to the extraordinary optical transmission will be treated, as well as dipole radiation and the presence of diffraction orders.

## 1.1 Surface Plasmon Polaritons

On the interface between a metal and a dielectric exist particular wave solutions for Maxwell's equations that are called Surface Plasmon Polaritons (SPPs), see chapter 12 of Novotny and Hecht [7] for an extensive description. They can be seen as waves of surface charge density oscillations of the free electrons in the metal. SPPs are excited by the oscillating electromagnetic field at discontinuities in the surface, for example slits or subwavelength holes.

SPPs are bound to the interface because of the optical properties of the two materials. The wavevector of a SPP depends on the relative permittivities of the dielectric ($\epsilon_d(\lambda)$) and the metal ($\epsilon_m(\lambda)$), these are wavelength dependent, but for readability this dependence will be implicit in the following. The relation between the wavevector of the incident light in free space ($k_0$) and the component of the wavevector of a SPP parallel to the surface ($k_{SPP}$) is called the dispersion relation [7]

$$k_{SPP} = k_0 n_{eff} = k_0 \sqrt{\frac{\epsilon_d \epsilon_m}{\epsilon_d + \epsilon_m}} \tag{1.1}$$

We consider only lossless dielectrics, so $\epsilon_d$ is real and positive. But the relative permittivity for metals is complex:

$$\epsilon_m = \epsilon_m' + i\epsilon_m'' \tag{1.2}$$

so also $k_{SPP}$ in Eq. 1.1 is complex. The real part of $k_{SPP}$ determines the wavelength of the SPP and the imaginary part accounts for the damping of the SPP as it travels along the surface. This damping results from ohmic losses of the electrons caused by the properties of the metal.

The component of the wavevector of a SPP perpendicular to the surface in the dielectric or metal ($k_{d,z}$ or $k_{m,z}$) is given by

$$k_{j,z} = k_0 \sqrt{\frac{\epsilon_j^2}{\epsilon_d + \epsilon_m}} \tag{1.3}$$

with $j = d, m$ and is also imaginary since $\epsilon'_m$ is negative and $|\epsilon_m|$ is larger than $|\epsilon_d|$. This means the SPP is bound to the surface and the field perpendicular to the surface is evanescent, as shown in Fig. 1.1

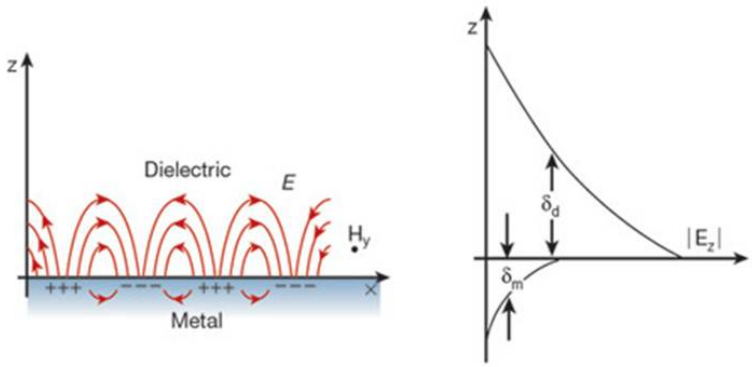


**Figure 1.1:** Schematic picture of the SPP on a metal-dielectric interface. The SPP travels parallel to the interface but the field normal to the interface is evanescent (from Barnes [8]).

As visible in Fig. 1.1 SPPs are purely transverse magnetic modes (TM), because of the metal properties. This means the H-field of the SPP wave is parallel to the surface and the E-field perpendicular.

Light coupled into a SPP at a metal-dielectric interface can travel over the surface for relatively long distances and can be coupled out into light again when encountering a discontinuity: more about this can be found in Sec. 1.3.

## 1.2 Dipole radiation

Light emitted, transmitted or scattered by subwavelength sources can in first approximation be described in terms of electric and magnetic dipoles [4]. An electric dipole can be seen as an alternating current with charges oscillating in one direction in an infinitesimal volume, while a magnetic dipole can be pictured as an alternating current circulating in an infinitesimally small ring. The radiation intensity patterns have the shape of a horn torus, as shown in Fig. 1.2, and neither of the dipoles radiates along it's axis.
The electric and magnetic fields of an electric dipole can be calculated (see Jackson [9])

$$\vec{\mathbf{B}}_e = k^2 \left(\hat{n} \times \vec{p}\right) \frac{1}{r} e^{ikr} \tag{1.4a}$$

$$\vec{\mathbf{E}}_e = \vec{\mathbf{B}}_e \times \hat{n} \tag{1.4b}$$

where $\vec{p}$ is the electric dipole vector, $k$ the wavevector of the radiation, $r$ the distance between the observer and the dipole and $\hat{n}$ the vector of the observing direction, as Fig. 1.2 shows. Eq. 1.4 are in cgs units. The $1/r$ dependence of Eq. 1.4 originates from the decrease of the fields with increasing distance and $e^{ikr}$ describes the oscillating behaviour of the fields.

The fields of a magnetic dipole are only slightly different:

$$\vec{\mathbf{E}}_m = -k^2 \left(\hat{n} \times \vec{m}\right) \frac{1}{r} e^{ikr} \tag{1.5a}$$

$$\vec{\mathbf{B}}_m = -\vec{\mathbf{E}}_m \times \hat{n} \tag{1.5b}$$

with $\vec{m}$ the magnetic dipole vector.

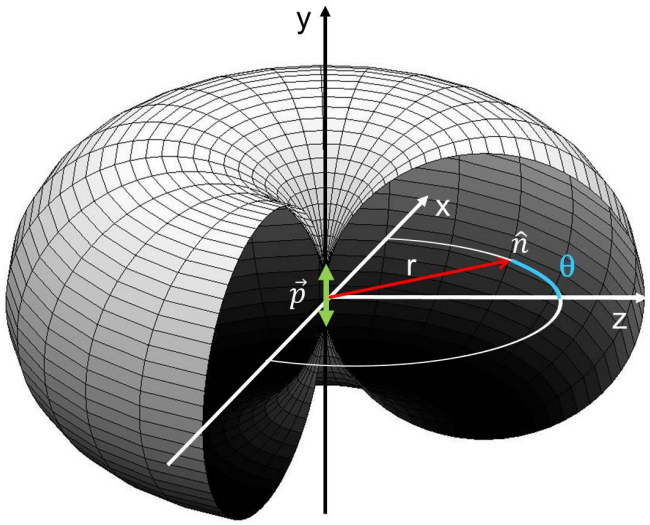


**Figure 1.2:** The radiation pattern of an electric dipole $\vec{p}$ at the origin oriented along the y-axis, when observing in direction $\hat{n}$ in the xz-plane at a distance r from the dipole.

We have six possible dipoles: both electric and magnetic dipoles in three orthogonal orientations (x,y,z). With Eq. 1.4 and Eq. 1.5 we can calculate the fields of the dipoles in the xz-plane: $|\vec{\mathbf{E}}| \propto cos(\theta)$ for $\vec{p}$ in x-direction, $|\vec{\mathbf{E}}| \propto 1$ for $\vec{p}$ in y-direction and $|\vec{\mathbf{E}}| \propto sin(\theta)$ for $\vec{p}$ in z-direction. The same relations hold for $\vec{m}$.

## 1.3 Extraordinary optical transmission and hole arrays

The extraordinary optical transmission (EOT) was discovered in 1998 by Ebbesen [2] on a sample consisting of a gold layer deposited on a dielectric (glass) perforated with arrays of subwavelength holes, similar to the sample used in this research and described in Sec. 2.1. In EOT transmitted light is composed of two contributions: the direct transmission through the holes and the light coupled into a SPP at one hole and coupled out into light at another hole. The SPPs cause the transmission to be higher than expected based on the transmission

through a single subwavelength hole as described by Bethe [1].
Since a definite phase delay exists between the two contributions the result is the effect of interference. Interference is only possible in case of both temporal and spatial coherence. The spectral resolution of the spectrometer $\Delta\lambda$ is small, which means $\Delta\nu$ is also small so $\Delta t$ is large enough for temporal coherence [6]. Because of a limited numerical aperture the coherence length of the incident light is larger than a SPP propagation length, so we also have spatial coherence [6].
The interference results in a spectral intensity variation with a typical Fano lineshape. The asymmetric lineshape of the Fano profile is caused by superposition of a constant background (by the direct transmission) and a Lorentzian resonance appearing due to the structure of the sample [5].
Eq. 1.1 can be rewritten to calculate the wavelengths $\lambda_0$ where Fano resonances will be visible in the transmission spectrum:

$$\lambda_0 = \frac{qa_0}{m}\sqrt{\frac{\epsilon_d\epsilon_m}{\epsilon_d + \epsilon_m}} \tag{1.6}$$

Where $qa_0$ gives the spacing of the holes in the array and $m$ is an integer originating from how many times the SPP fits in the spacing between two holes. The higher the value of q, the more resonances appear in the transmission spectrum. The resonance wavelengths from Eq. 1.6 are closer to the minimum of the corresponding Fano profile than to it's maximum.

The interference of these two contributions is also incorporated in the microscopic model proposed by Liu and Lalanne to describe the transmission $T$ through an array of subwavelength holes, when considering direct transmission and SPPs [5]

$$T(\lambda) = \left| t_0(\lambda) + \frac{2\ \alpha\beta(\lambda)}{e^{-ik_{SPP}qa_0} - (\rho + \tau)} \right|^2 \tag{1.7}$$

In this equation $t_0$ is the direct transmission through the holes, $\beta$ a coefficient describing the probability for an incident plane wave to couple into a SPP and $\alpha$ a coefficient for the probability for a SPP to couple out into light on the other side of the sample. These two are taken together in $\alpha\beta$ describing the in- and outcoupling of light and SPPs. The exponential $e^{-ik_{SPP}qa_0}$ describes the phase shift experienced by a SPP in one period $qa_0$, $\rho$ is a coefficient for the probability that a SPP is reflected when it encounters a hole and $\tau$ for the probability that the SPP is transmitted into a plasmon again. This is clarified in Fig. 1.3.

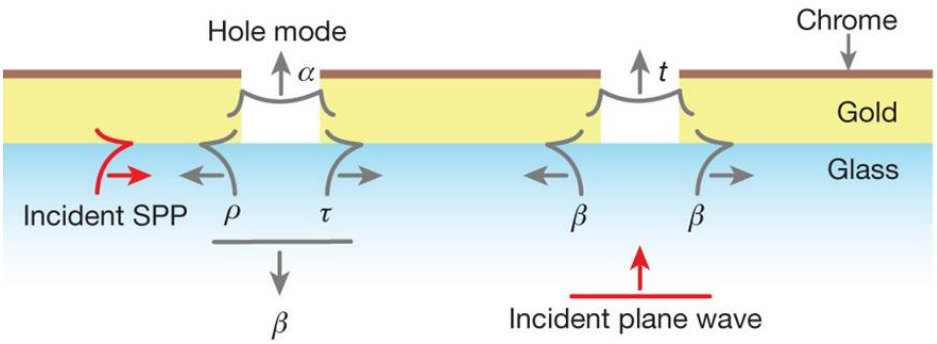


**Figure 1.3:** Scattering processes on the sample. Left: a SPP encountering a hole can be reflected ($\rho$), transmitted ($\tau$), coupled back into light ($\beta$) or coupled out into light on the other side ($\alpha$). Right: a plane wave can be coupled into a SPP ($\beta$) or be transmitted ($t = t_0$) (from van Beijnum [6]).

It was demonstrated by van Beijnum [6] that SPPs are not the only origin of the EOT for our kind of samples. When a propagating wave encounters a subwavelength hole it not only excites SPPs but it is also scattered by the hole. This diffracted field is called quasi-cylindrical wave (QCW) because it's characteristics are like those of a free-space cylindrical wave [5]. This QCW is not bound to the surface, but propagates in all directions, including the direction parallel to the metal-dielectric interface. While creeping at the surface over a certain distance it can also interact with other subwavelength holes and increase the transmission, like SPPs do.
At optical wavelengths SPPs and the QCW are both excited, but the damping length of the QCW is much shorter that that of SPPs (about 700 nm [6] and 10 $\mu$m [2] respectively for gold). This means the contribution to the EOT by the QCW is more significant if the spacing between the holes is less than the damping length.

## 1.4 Diffraction orders

A sample with a regular pattern of subwavelength structures acts as a grating, so it generates diffraction orders. For our experiment we are interested in the intensity of the transmitted light in these orders, so we need to know at which angle they appear. The positions of diffraction orders can be calculated using the grating equation [7]

$$sin(\theta_n) = sin(\theta_{in}) + \frac{n\lambda}{qa_0} \tag{1.8}$$

with $\theta_n$ the angle where we expect the n$^{th}$ diffraction order of wavelength $\lambda$, $qa_0$ corresponds to the spacing between the holes (as explained in Sec. 2.1) and the angle of incidence $\theta_{in}$ is zero in our experiments because we used normal incidence.

Since $\theta_n$ is wavelength-dependent and our experiment was performed using a white light source, angular dispersion $D$ occurs. For normal incidence this is defined as

$$D \equiv d\theta/d\lambda = \frac{n}{qa_0 cos(\theta_n)} \tag{1.9}$$

which means the angular separation of two wavelengths increases as the order n increases [7]. Because of this phenomenon the spectra in diffraction orders are smeared out in space and cannot be measured entirely at only one angle.

Novotny and Hecht [7] give the equation for the intensity distribution for diffraction by many slits ($N$) with spacing $a$ and width $b$:

$$I(\theta) = I_0(\theta) \left( \frac{sin(\beta)}{\beta} \right)^2 \left( \frac{sin(N\alpha)}{\alpha} \right)^2 \tag{1.10}$$

with $\alpha = k\,a\,sin(\theta)/2$ and $\beta = k\,b\,sin(\theta)/2$. In Eq. 1.10 $\left(\frac{sin(N\alpha)}{\alpha}\right)^2$ is the interference term, which can be seen as the structure factor. It originates from the structure of the grating, so in our case from the spacing $qa_0$ between the holes (see Sec. 2.1).
$\left(\frac{sin(\beta)}{\beta}\right)^2$ is the diffraction term. If $b$ is very small (which was the case for our sample) then is $\frac{sin(\beta)}{\beta} \approx 1$ and all diffraction orders are approximately equally intense.
$I_0(\theta)$ can be seen as the form factor and depends on expansion in dipoles of the transmission.

## 1.5 Theory for this project

We are interested in the strength and orientation of the electric and magnetic dipoles describing the EOT through our sample. Therefore we will look at the angle dependence of the total transmission through the sample and the angle dependences of both the direct transmission ($t_0$) and the contribution of SPPs ($\alpha\beta$).

In Sec. 1.2 we introduced the equations to calculate the electric and magnetic fields of dipoles. In case of a combination of dipoles the fields add up. Dipoles in z-direction have anti-symmetric fields in the xz-plane and the radiation patterns become asymmetric when added to other fields. We expect symmetric radiation patterns at positive and negative angles because the diffraction orders are symmetric, so we exclude the dipoles in z-direction. A better theoretical justification of this exclusion is currently being worked on.
This means that only the constant term and the $cos(\theta)$ term remain and these have to be added up with a phase difference $\phi$ between the radiation of the electric and magnetic dipoles. The radiation intensity pattern in the xz-plane can be described as:

$$I(\theta) = A \left| 1 + \sqrt{B}\, cos(\theta)\, e^{i\phi} \right|^2 \propto 1 + B\, cos^2(\theta) + 2\sqrt{B}\, cos(\theta)\, cos(\phi) \tag{1.11}$$

where $A$ and $B$ depend on the strength and orientation of the different dipoles. In Eq. 1.11 we see that the ratio of the fields of the electric and magnetic dipoles can be calculated from the square root of B.

Rotenberg showed that the magnetic polarizability of a hole $\alpha_M$ is larger than the electric polarizability $\alpha_E$ [4]. So we expect the induced magnetic dipoles to be stronger and contribute more to the transmission than the electric dipoles. This will influence the values of $B$.

According to Sec. 1.2 also the direct transmission ($t_0$) and the contribution of the SPPs

$(\alpha\beta)$ can be expanded in terms of electric and magnetic dipoles and both depend on the angle of observation $\theta$ in the scanning plane (see Fig. 2.4 in Sec. 2.2).

Yi and Ebbesen [10] showed the angle dependence of the direct transmission through one hole ($t_0$). They measured the far field diffraction patterns of a single, subwavelength, circular aperture scanning a fixed xz-plane with both s- and p-polarization. P-polarization is defined in the scanning plane and s-polarization perpendicular to the scanning plane. Different models are used to describe the angle dependence of the normalized intensity $I(\theta)$.
They start with the equations for the normalized intensity for a real metal with a single hole. In the supplementary information of [10] the limit for subwavelength holes ($kr \to 0$) is used to obtain a dipole expansion for $I(\theta)$:

$$I_p^{dip}(\theta) = \frac{|1 + z_s|^2 cos^2(\theta)}{|cos(\theta) + z_s|^2} \tag{1.12a}$$

$$I_s^{dip}(\theta) = \frac{|1 + z_s|^2 cos^2(\theta)}{|1 + z_s cos(\theta)|^2} \tag{1.12b}$$

with $\theta$ the angle of observation and $z_s = 1/\sqrt{\epsilon_m}$ the impedance of the metal.
Assuming both subwavelength holes ($kr \to 0$) and a perfect electric conductor (PEC, for which $z_s \to 0$) the equations are the same as Bethe derived in 1944 [1]:

$$I_p^{bethe}(\theta) = 1 \tag{1.13a}$$

$$I_s^{bethe}(\theta) = cos^2(\theta) \tag{1.13b}$$

In the paper of Yi and Ebbesen it is demonstrated how these models fit the data. For s polarization all models are approximately similar and fit the data quite well. For p polarization the models are very different and none of them fits the data very well, but Eq. 1.12 fits better than Eq. 1.13.
Based on these models we expect the normalized intensity of the direct transmission to show a $cos^2(\theta)$ dependence for s polarization. For p polarization the normalized intensity will be more constant with angle, but not independent of angle as Bethe showed, since we have a real metal and holes with a non zero diameter.

# Chapter 2

# Materials and methods

The goal of the experiment was to measure the amount of light transmitted through the sample at different wavelengths and at angles corresponding to the diffraction orders.
In this chapter we describe how the experiments were performed in order to obtain these data. We will treat the sample, the experimental setup, the data acquisition and the data analysis.

## 2.1 Sample

All experiments were performed with a sample containing regular arrays of subwavelength holes in a gold film. The 150 nm thick layer of gold is deposited on a glass substrate and covered with a 20 nm layer of chromium (this is visible in Fig. 1.3). This additional layer of chromium has the purpose of damping the SPPs on the air-side of the gold so we can study the effects of SPPs on the gold-glass interface only. Chromium damps SPPs because the imaginary part of it's relative permittivity is large compared to the real part (E.D.Palik, "Handbook of Optical Constants of Solids" (1985)).
On the gold film 14 square samples are present with a size of 400 $\mu$m. Because all samples are on the same substrate, the thickness of the gold can considered to be constant. The 14 samples contain arrays of circular holes with a diameter of 162$\pm$4 nm [6]. The arrays can be seen as rows of holes spaced by $a_0 = 450$ nm in y-direction. The distance between these rows in x-direction is $qa_0$, where q is different for all samples ($q = 1, 2, 3, ..., 10, 12, 14, 16, 18$), as shown in Fig. 2.1 for the $3a_0$ array. Because of the rectangular patterns of holes the sample acts as a grating according to Sec. 1.4 and diffraction orders were present.
A preliminary survey of the sample at the optical microscope revealed that some of the arrays were damaged; for this reason it was not possible to use samples with spacing $4a_0$, $5a_0$ and $7a_0$.

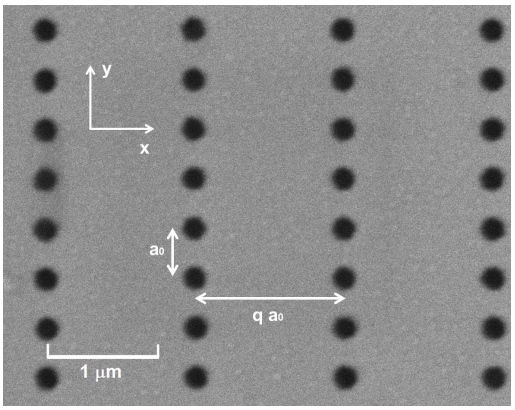


**Figure 2.1:** SEM image of the $3a_0$ sample with a magnification of 65000. The spacing between the holes in x and y-direction is indicated (q=3 in this case).

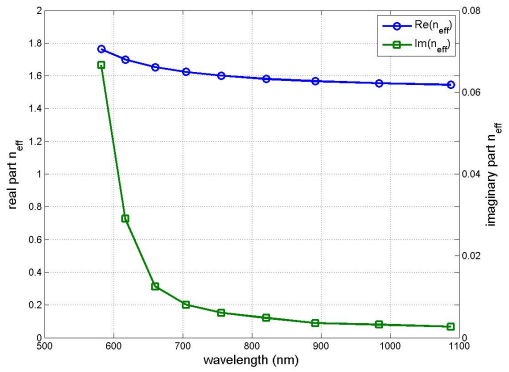


**Figure 2.2:** Plot of the real and imaginary part of the wavelength dependent effective refractive index for the gold-glass interface of our sample. The imaginary part is very small compared to the real part.

In Sec. 1.1 it was shown that according to Eq. 1.1 the wavevector of the SPP depends on the relative permittivities of the glass and the gold. The glass substrate of this sample is Schott N-BK7 glass with a refractive index of 1.51, equivalent to $\epsilon_d = n^2 = 2.28$. This refractive index changes less than 1% in our wavelength range so we consider it constant.
The relative permittivity of the gold was calculated using data of Johnson and Christy [11]. This gives an effective refractive index which is wavelength dependent, as shown in Fig. 2.2.

## 2.2 Experimental setup

Fig. 2.3 shows a schematic picture of the setup.
The setup consists of two parts: the illumination optics fixed to the optic table and the detection optics mounted on a rotating arm. White light from an OceanOptics halogen lamp (HL-2000-HP-FHSA) was coupled into a 200 $\mu$m multi-mode fiber and imaged onto the sample by the illumination optics. This imaging was performed by a 4f-configuration using a $f_1$=50 mm lens (LB 1471) and a $f_2$=75 mm achromatic doublet lens. The lenses were chosen to obtain a magnification of 1.5 for the imaging, so the spot on the sample had a diameter of 300 $\mu$m which fits on the 400 $\mu$m square samples.
The sample was imaged on a 400 $\mu$m multi-mode fiber after a $\frac{2}{3}$ magnification by the detection optics. This contained a second 4f-configuration consisting of two achromatic doublet lenses ($f_1$=50 mm and $f_2$=75 mm). Achromatic doublet lenses were necessary since we worked with a white light source. Normal lenses can give chromatic aberration effects, while achromatic doublets have a focal length independent of the wavelength. This was necessary for focusing light into the detection fiber. For the first lens, which only had to produce a parallel beam, chromatic abberation was less of a problem so in that position we could use a normal lens. We used the Thorlabs AC 254-075-B-ML for the $f_2$=75 mm lenses and the AC 254-050-B-ML for the $f_1$=50 mm lens.

Apertures were placed in both arms to control the numerical aperture (NA) of the beam. The used NA should be small to reduce the spread in k-vector to prevent the excitation of

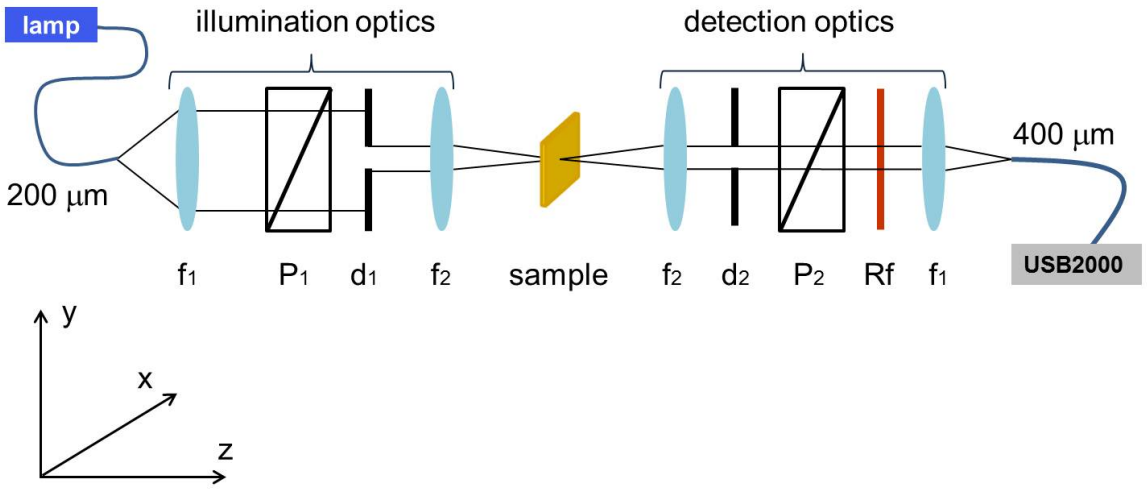


**Figure 2.3:** Schematic picture of the setup. White light from the halogen lamp is coupled into a 200 $\mu$m fiber and imaged onto the sample by two lenses ($f_1$=50 mm and $f_2$=75 mm). The transmitted light is imaged by the detection optics onto the 400 $\mu$m fiber leading to the USB2000 spectrometer. The NA and polarization can be controlled with apertures $d_1$ and $d_2$ and polarizers $P_1$ and $P_2$. The redfilter (Rf) filters out all the light for wavelength smaller then 580 nm.

unwanted resonances.
The diameter of the first aperture $d_1$ was 1.5 mm, which combined with $f_2$=75 mm gives a NA of 0.01 for our setup. The second aperture was set to $d_2$=10 mm to collect most of the diffracted light, which is spread out in space by angular dispersion as described in Sec. 1.4.

Polarizers are placed in both arms to control the polarizations of the incident and transmitted beam. The polarization of the incident light determines the direction of propagation of the SPPs. SPPs excited by for example horizontally polarized light will travel in horizontal direction along the surface of the metal. This provides an easy way to control the main direction of propagation of the SPPs during the experiment.
The used polarizers are B. Halle Glan Thompson polarizing prisms, with an extinction ratio better than $10^{-8}$ and a deformation of a transmitted plane wave less than $\lambda/10$. The polarizers were placed in a precision rotation stage (Thorlabs CRM1P) so they could be rotated with a 5 arcmin resolution.
We defined p-polarization as the polarization along the x-axis (also called a TM wave) and s-polarization along the y-axis (TE wave). The polarization more frequently used in other research is p-polarization so we'll use it to compare our results with previous works. With two polarizers we could measure in four configurations: pp, ss, sp and ps.

All experiments in this thesis were performed in pp or ss configuration but we also measured a few transmission spectra in the ps configuration. The extinction ratio with crossed polarizers was $10^{-4}$ and we obtained spectra that looked a lot like those in the pp configuration, but differ by a factor $10^{-3}$. This means the depolarization is less than 0.1%.

The spectrometer used for the data aquisition was an OceanOptics USB2000. This spectrometer has a wavelength range from 200 nm to 1100 nm, this includes the range between

650 nm and 950 nm we were interested in.
This CCD based spectrometer contains 2048 effective pixels, giving a spectral resolution of about 0.44 nm/pixel. We checked the wavelength scale of the spectrometer with a green laser pointer (532 nm), looking at both the main 532 nm peak and its first order at 1064 nm.
The USB2000 operates with a grating, which produces diffraction orders. Because of this grating the second diffraction order of for example a 550 nm peak ends up on the 1100 nm pixel, leading to a wrong interpretation of the spectrum. To prevent this from happening we used a longpass redfilter to cut off all the light below 580 nm.

The rotating stage with the detection optics was controlled by an ESP300 controller using LabView, with an accuracy for the rotation angle better than 0.01°. The stage was free to rotate from -40° to 90° without clashing with another part of the setup.
Both illumination and detection optics were aligned by connecting the lamp to the fibers and checking that the foci were on the rotation axis independent of the position of the rotating stage.

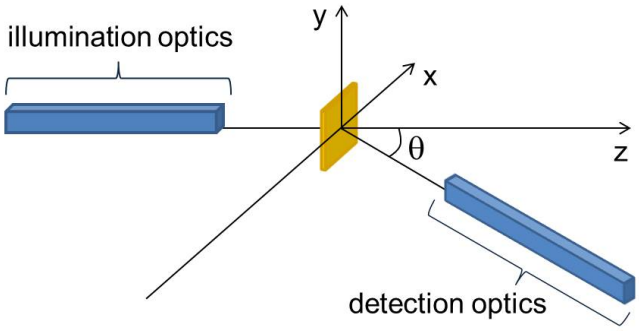


**Figure 2.4:** The definition of the angle $\theta$ in the xz-plane where a measurement is performed.

The orientation of the sample is an important factor in these measurements. For this reason we designed a sample holder which allowed us to control rotation around the x-, y- and z-axis. We needed to know the k-vector of incident light with respect to the plane of the sample: we checked for normal incidence by centering the reflection of the illumination beam at the center of the first aperture $d_1$ rotating over the x- and y-axis. A CCD camera was used to check whether the diffraction orders appear at the same height, this depends on the z-axis rotation.

Usually in research on SPPs the metal-dielectric sample is illuminated from the dielectric side. During most of our experiments we illuminated from that side, but we also did series of measurements with illumination on the chromium side of the sample and detection on the glass side.

## 2.3 Data acquisition

Two methods were used to obtain data:

Method A: Move the detection arm to the correct angle for a certain wavelength and diffraction order and save the measured spectra with the program SpectraSuite. This method could be used to look at the angle dependence of the intensity of a certain wavelength, but it was impossible to obtain the complete spectrum at higher diffraction orders because of angular dispersion. Multiple spectra were taken and averaged to improve the signal to noise ratio.

Method B: Scan the whole ($\lambda$,$\theta$) plane with small angle steps. From the obtained 3D data set (an example is shown in Fig. 2.5) we could extract the complete spectra for the diffraction orders.

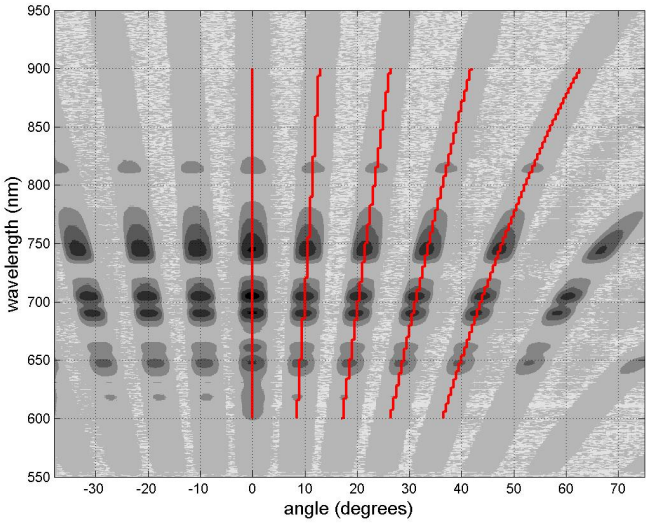


**Figure 2.5:** Example of a 3D map obtained with method B for the $9a_0$ array in the pp configuration. The red lines show where the spectra for diffraction orders n=0-4 that were extracted.

To calculate the transmission $T$ from the measured spectra we needed to compare the light passing through the sample with a reference beam. This was obtained by moving the sample out of the beam using a stage and measuring the spectrum of the lamp. A dark signal was measured and subtracted from all spectra.

## 2.4 Analysis of the data

The transmission spectra were calculated using the following equation:

$$T = \left(\frac{t_L}{t_S}\right) \frac{S - D_S}{L - D_L} \tag{2.1}$$

where $t_S$ and $t_L$ are the different integration times for respectively the light through the sample ($S$) and the reference beam ($L$). Dark signals $D_S$ (for $S$) and $D_L$ (for $L$) were measured

with the same integration times $t_S$ and $t_L$.

Calculated transmission spectra can be fitted with Eq. 1.7 using the approximate wavelength dependences: $t_0 \propto \lambda^{-2}$ and $\alpha\beta \propto \lambda^{-4}$ together with five free parameters [6].
Then the fitting equation becomes:

$$T(\lambda) = \left| \left(\frac{\lambda_0}{\lambda}\right)^2 p_1 + \left(\frac{\lambda_0}{\lambda}\right)^4 \frac{p_2\, e^{ip_3}}{e^{-i\, k_{SPP}\, q a_0} - p_4\, e^{ip_5}} \right|^2 \tag{2.2}$$

The fits were performed using the least squares method in Matlab. For $\lambda_0$ we took 800 nm, which is close to the resonance wavelength, $k_{SPP}$ was calculated with Eq. 1.1 and the effective refractive index from [11].
Fitting Eq. 2.2 to the diffraction orders could give information about the angle dependence of the direct transmission ($p_1(\theta) = t_0$) and the resonant contribution to the transmission ($p_2(\theta) = |\alpha\beta|$), which we are interested in. $p_1(\theta)$ and $p_2(\theta)$ depend on the angle of observation but $p_4 = |\rho + \tau|$ contains information about processes on the sample and should be constant for the spectra from different diffraction orders. $p_3$ and $p_5$ are phases, these do not give us the information we need.

Two different methods were used to extract information from the data:

The first method comparing the transmission in the diffraction orders at the wavelength where the peak of a resonance was located. These transmissions were normalized by the transmission in first order and plotted as a function of the angle. We divide by the first order because the zeroth order also includes light transmitted through the gold film (as will be discussed in Sec. 4.3) and the angles of the first orders for different arrays are close enough to each other.
The plot of normalized transmission versus angle is fitted with Eq. 1.11 using the least squared method in Matlab and two free parameters ($B$ and $\phi$).
The advantage of this method is that the angular dispersion does not cause a problem. A disadvantage is that only the total transmission is obtained, while we are also interested in the direct transmission and the resonant contribution separately.

The second method fitting Eq. 2.2 to the transmission spectra of the diffraction orders to separately determine the direct transmission ($t_0$) and the resonant contribution ($|\alpha\beta|$). These parameters were normalized and plotted as a function of angle. To make accurate fits, full spectra were necessary in all diffraction orders, so we needed the data acquired with method B.

# Chapter 3

# Experiments zeroth order transmission

We will compare the zeroth order transmission spectra we obtained with those measured in 2010 (see [6]) on exactly the same sample. The two experiments can be compared because the same lamp, optics, magnification and polarization were used in both cases.
Measurements were performed on three different arrays of holes and we fitted Eq. 2.2 to the spectra to learn more about the processes contributing to the EOT.

## 3.1 Results and fitting of the two measurements

We show the zeroth order transmission from previous measurements in 2010 (Fig. 3.1(a)) and our recent measurements (Fig. 3.1(b)). In both cases spectra were obtained for three different arrays with hole spacing $2a_0$, $3a_0$ and $6a_0$ and Eq. 2.2 was fitted to the data. The fitting was performed on the whole set of data (all three spectra together).
The polarizer in the illumination optics was in p configuration during the experiments so SPPs propagated mainly in $qa_0$ direction and the polarizer in the detection optics was removed.
If we compare the two graphs in Fig. 3.1 we notice that the transmission is higher in our measurements by approximately a factor 2.5. The peaks of the resonances are broader and the peak positions of the resonances have shifted to longer wavelengths.

The fitting parameters corresponding to the fits in Fig. 3.1(a) and Fig. 3.1(b) are displayed in table 3.1:

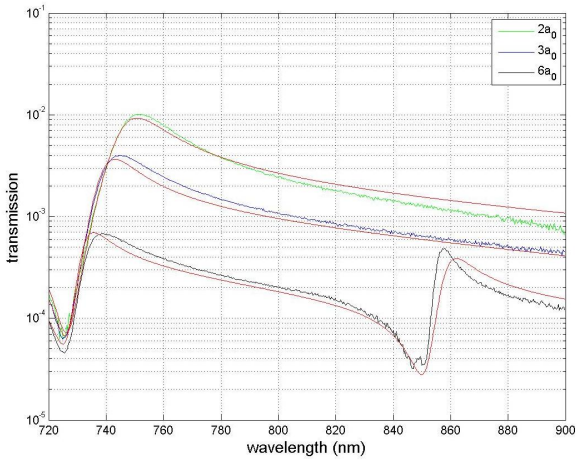


(a)

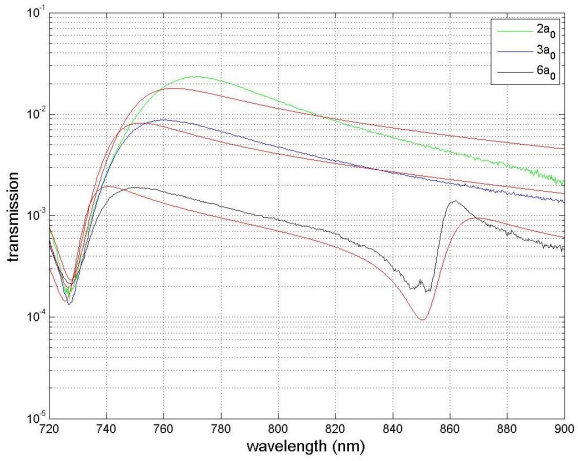


(b)

**Figure 3.1:** The zeroth order transmission spectra and fits of Eq. 2.2 (red lines) for arrays with hole spacing $2a_0$, $3a_0$ and $6a_0$. (a) shows the old measurements from 2010 and (b) our recent measurements.

| parameter | fits from 2010 | | | our fits | | |
|---|---|---|---|---|---|---|
| $p_1 = t_0$ | 0.074 | $\pm$ | 0.001 | 0.146 | $\pm$ | 0.003 |
| $p_2 = \lvert\alpha\beta\rvert$ | 0.024 | $\pm$ | 0.001 | 0.054 | $\pm$ | 0.002 |
| $p_3 =$ phase of $\alpha\beta$ | 2.13 | $\pm$ | 0.04 | 2.46 | $\pm$ | 0.07 |
| $p_4 = \lvert\rho + \tau\rvert$ | 0.86 | $\pm$ | 0.01 | 0.72 | $\pm$ | 0.02 |
| $p_5 =$ phase of $\rho + \tau$ | 0.42 | $\pm$ | 0.02 | 0.49 | $\pm$ | 0.05 |

**Table 3.1:** Overview of the fitting parameters and corresponding errors for the old and new measurements.

## 3.2 Discussion

The sample used for our experiments was produced more than three years ago and the measurements from [6] were also performed three years ago. From our measurements we have evidences that it's properties have changed. If we compare Fig. 3.1(a) and Fig. 3.1(b) we see redshifted peaks, increased transmission and broader peaks in our spectra compared to those from 2010.
The fits of Eq. 2.2 to the data are not as good as they were for the old measurements. Therefore we cannot draw hard conclusions from the fitting parameters in table 3.1. But we can see that both the direct transmission $t_0$ and the resonant contribution $|\alpha\beta|$ differ by a factor two. This means higher direct transmission and stronger coupling of light into SPPs and vice versa, which is in accordance with the higher transmission we observed. The parameter describing the transmission and reflection of SPPs ($|\rho + \tau|$) is lower for our fits. The lower this parameter, the more losses and the broader the resonance, which is also in accordance with our data.

These results suggest that the sample has changed. There are a few possible explanations for the observed changes: (i) the holes might have been filled with a material with a refractive index different from that of air, (ii) chromium of the top layer might have diffused into the gold and thus changed the effective refractive index, (iii) the diameter of the holes might have increased.
We wanted to find out more about the origin of the changes. High resolution SEM images of the sample could be used to estimate the hole size and check whether this has changed. In Fig. 3.2 we show an image of a hole with a 50000 magnification. The edges of the holes on this image are indistinct so the image itself gives no proof that the hole size has changed but it shows evidences that the holes are not circular anymore. In turn, the analysis of intensity profile in Fig. 3.3 suggests that the diameter has increased. We show that the diameter is at least 181 nm while in 2010 it was estimated to be 165 nm. Even this modest 10% increase can have large consequences for the transmission since theory predicts $T \propto a^6$ with a the hole size [1].

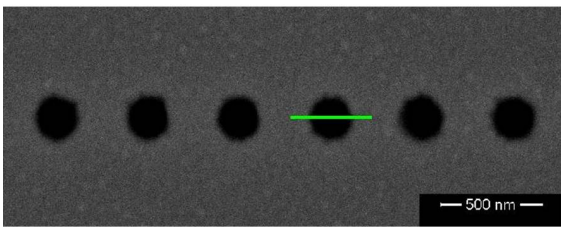


**Figure 3.2:** SEM image with a 50000 magnification of circular holes on the $10a_0$ array.

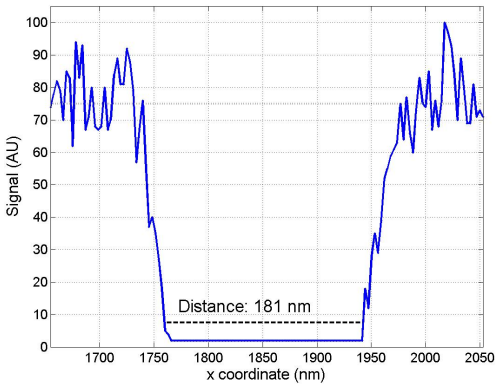


**Figure 3.3:** Plot of the intensity along the green line in Fig. 3.2 to estimate the hole size.

Cleaning the sample could remove material that has filled the holes. After cleaning could be checked whether the spectra are more similar to those from [6].

# Chapter 4

# Experiments pp configuration

We measured the transmission through four different hole arrays with both polarizers in x-direction (see Fig. 2.4), so in the pp configuration. This means the SPPs propagated mainly in the $qa_0$ direction (x-direction) on the sample.
Transmission spectra were obtained in the diffraction orders for four different hole arrays while illuminating the sample from the glass side. We calculated the normalized intensities and analyzed these by looking at the angle dependence of the transmission at a certain wavelength. To learn more about the angle dependence of the direct transmission and the resonant contribution by SPPs we fitted Eq. 2.2 to the spectra.

## 4.1 Results

Transmission spectra were obtained for arrays with hole spacing $6a_0$, $8a_0$, $9a_0$ and $10a_0$. We used these arrays because they provide enough diffraction orders and the intensity is high enough for a good signal to noise ratio. Spectra in the diffraction orders were measured both by positioning the rotating stage at the angles of the diffraction orders for the resonances wavelengths (method A, as described in Sec. 2.3) and by acquiring the whole spectrum at each angle with steps of $0.5^\circ$ and extracting the diffraction orders (method B).
The spectra for the array with spacing $9a_0$ obtained with method A are shown in Fig. 4.1 and those for method B in Fig. 4.2. For clarity only spectra of the zeroth order and first four diffraction orders are displayed. We show the results for $9a_0$, but the other arrays give similar spectra.

In all spectra the Fano lineshapes of the resonances are clearly visible. The theoretical positions of the resonances can be calculated with Eq. 1.6: the resulting wavelengths are closer to the minimum than to the maximum of the Fano lineshape. The resonance for spacing $9a_0$ in Fig. 4.1 and Fig. 4.2 in the middle of our wavelength range is positioned at 726 nm and originates from SPPs that fit 9 times in the spacing between two holes. This shape at 726 nm is visible in spectra for all different hole arrays, originating from SPPs which fit q times in the hole spacing. In the analysis we will focus on this resonance because it is present in all spectra.
Other Fano lineshapes are visible in Fig. 4.1 and Fig. 4.2 at 665 nm and 804 nm. With Eq. 1.6 we calculated that these correspond to SPPs fitting respectively 10 or 8 times in the $qa_0$ hole spacing.

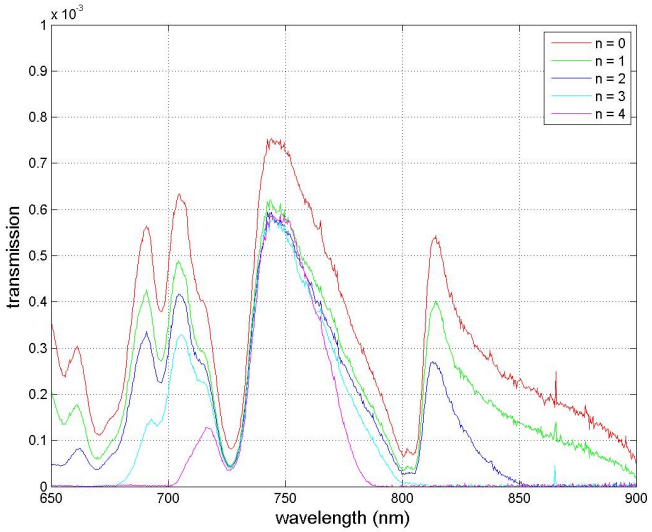


**Figure 4.1:** Transmission spectra for the array with spacing $9a_0$ in the pp configuration measured with method A.

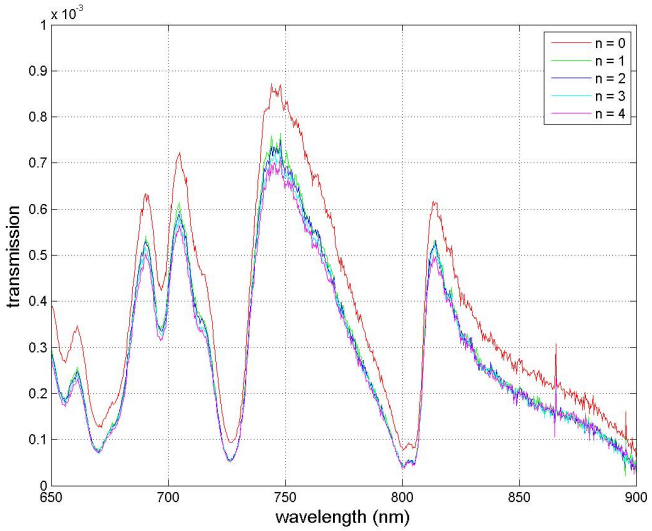


**Figure 4.2:** Transmission spectra for the array with spacing $9a_0$ in the pp configuration measured with method B.

In Fig. 4.1 and Fig. 4.2 it is visible that the zeroth order is more intense than the other orders, so there might be some contribution to only the zeroth order. This could be the direct transmission through the gold layer between the holes, since this would only be visible in the zeroth order. The transmission through the gold was measured and varies from $3 \cdot 10^{-6}$ to $7 \cdot 10^{-6}$ in our wavelength range. This can interfere constructively or destructively with the transmission through the holes and we calculated that it could increase the transmission through the sample with approximately 5% in case of constructive interference.

We can see in Fig. 4.1 that the spectra for higher orders are cut off because of angular dispersion when using method A. Fig. 4.2 shows that all spectra are complete for method B.

To visualize the angle dependence of the transmission we use normalized intensities so we can compare results of samples with different hole spacing. The normalized intensity was calculated by dividing the transmission at a certain wavelength in all diffraction orders by the transmission of the first order. We divide by the first order since the zeroth order is different from all other orders.
The normalized intensities are calculated at 748 nm (the position of the peak of the resonance at 726 nm) and the results for the four different arrays are plotted as a function of angle in Fig. 4.3 and Fig. 4.4.
The effect of the incomplete spectra in Fig. 4.1 will not be visible in Fig. 4.3 and Fig. 4.4 because we look at the intensity at only one wavelength in the diffraction orders.

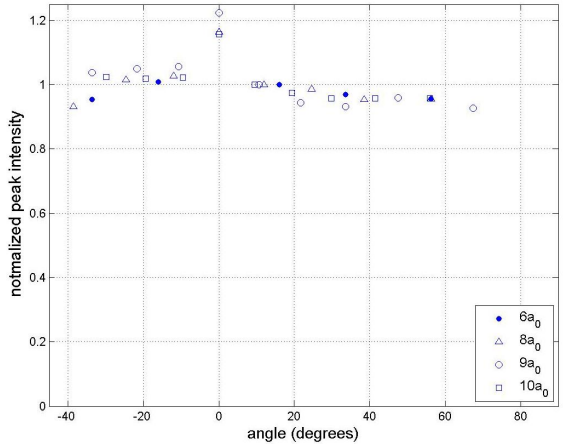


**Figure 4.3:** Normalized peak intensities at 748 nm for the diffraction orders of arrays with spacing $6a_0$, 8, 9 and $10a_0$ measured with method A.

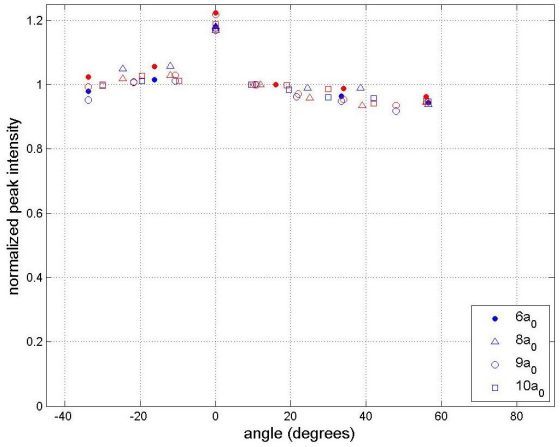


**Figure 4.4:** Normalized peak intensities at 748 nm for the diffraction orders of arrays with spacing $6a_0$, 8, 9 and $10a_0$ measured with method B. Two sets of data from a repetition of measurements are plotted, in red and blue to distinguish them.

In both Fig. 4.3 and Fig. 4.4 we can see that the normalized peak intensities do not have a strong angle dependence, irrespective of the method used as normalized intensities show only a 5% variation over 50°.

Looking at the data we noticed an asymmetry between the intensities at positive and negative

angles. In all measurements we obtained a higher intensity at negative angles. This is most probably caused by a problem with the alignment, because the asymmetry is the same when we rotate the sample 180° over the z-axis or y-axis. We reduced this effect by improving the alignment of the setup, but still have some asymmetry.
We analyzed the first diffraction orders with a CCD. In Fig. 4.5 we show that the image for $n = -1$ is not an oval shape as expected but has a strange shape with a streak in y-direction. The image for $n = 1$ in Fig. 4.6 is a oval shape.
Because of the asymmetry we will only use the spectra of diffraction orders obtained at positive angles in the analysis of the data in this thesis.

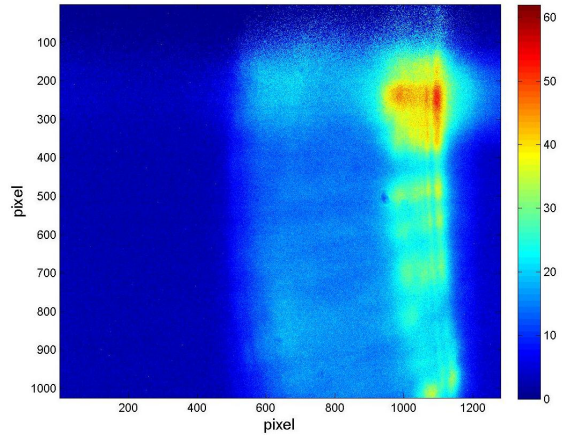


**Figure 4.5:** CCD image of n = -1 for the $9a_0$ array. We expected an oval shape, but some streak is visible ($\theta = 0$ is on the right).

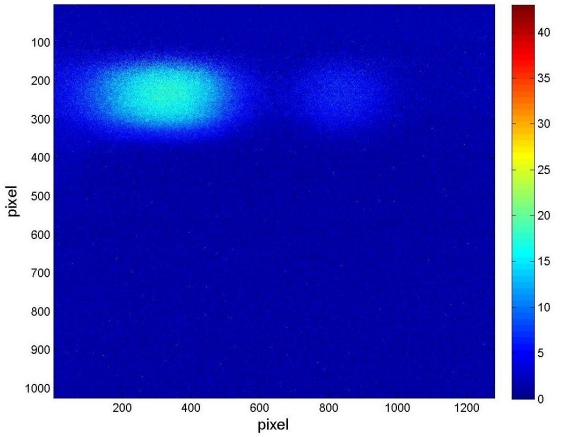


**Figure 4.6:** CCD image of n = 1 for the $9a_0$ array, this image is an oval shape as expected ($\theta = 0$ is on the left).

## 4.2 Analysis

The data in Fig. 4.4 give the dependence in $\theta$ of the intensity transmitted by the holes; for this reason it is possible to apply to them the model of interfering electric and magnetic dipoles explained in Sec. 1.5.

We fitted Eq. 1.11 to the data from Fig. 4.4 for positive angles, excluding the zeroth order, and the results of the fitting are shown in Fig. 4.7.
This gives $B = 0.4 \pm 0.2$ and $\phi = 2.0 \pm 0.2$ rad. With this value we can calculate the ratio of the fields of the electric and magnetic dipoles to be $\frac{E_m}{E_p} = 1.6 \pm 0.3$, which means that the magnetic dipole radiation seems stronger, as was also predicted by Rotenberg [4].

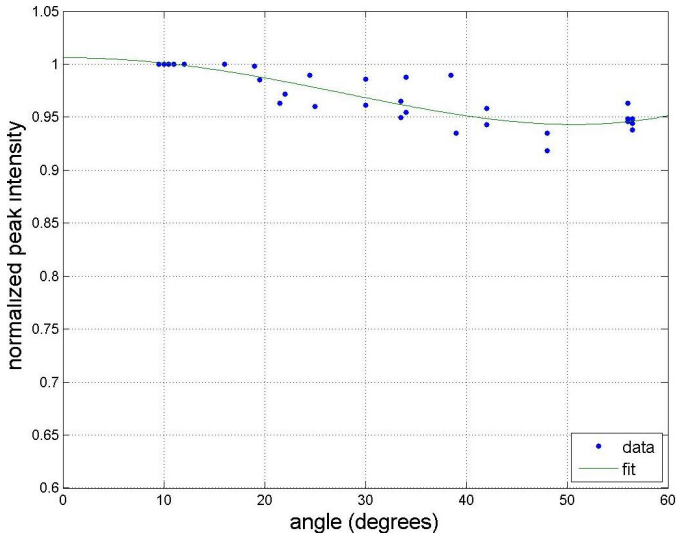


**Figure 4.7:** Data from Fig. 4.4 for positive angles with the fit of the dipole model (Eq. 1.11).

Until now we treated the total transmission through the sample, but we are also interested in the angle dependence of both the direct transmission and the resonant contribution by SPPs. That information can be extracted from Fig. 4.2 by fitting Eq. 2.2 to the spectra. The fitting is performed on the data obtained with method B because those are complete spectra, which is necessary for good fits. We fitted the zeroth order and positive diffraction orders for arrays with hole spacing $6a_0$, $8a_0$, $9a_0$ an $10a_0$. In Fig. 4.8 the spectra and fits for the array with spacing $10a_0$ are shown in the wavelength rage from 715 nm to 880 nm.

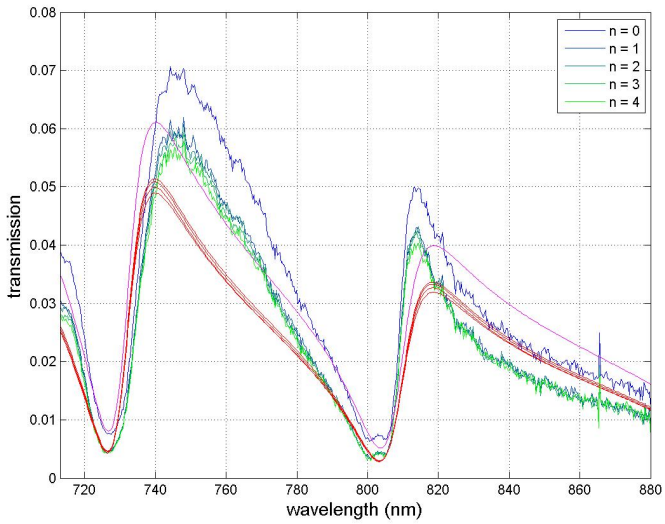


**Figure 4.8:** The fits of Eq. 2.2 to spectra of the $9a_0$ array for the positive diffraction orders. The spectra are shown in blue and green, the fit in magenta for the zeroth order and in red for the higher orders.

The fits in Fig. 4.8 suffer from the same problem reported for zeroth order spectra in previous chapter, making it difficult to draw hard conclusions. The fits give the correct positions

for the minima of the resonances, but they underestimate the transmission and the peak positions are not correctly fitted. This might be because the properties of the sample have changed (as discussed in Sec. 3.2) so the values for $k_{SPP}$, $n_{eff}$ or $a_0$ we used in the fitting function 1.7 might not be correct anymore.

The model fails in correctly fitting the peaks of the spectra but the minima are at the correct wavelengths, so an attempt can be done to extract information from the fitting. Five parameters are obtained from the fitting and we are interested in the direct transmission ($p_1(\theta)$) and the resonant contribution by the SPPs ($p_2(\theta)$). We normalize the parameters by dividing $p_1(\theta)$ and $p_2(\theta)$ for a certain array by the value in the first diffraction order for that array.
The normalized fitting parameters for fits to the arrays with spacing $6a_0$, $8a_0$, $9a_0$ and $10a_0$ are plotted as a function of angle in Fig. 4.9 and Fig. 4.10.

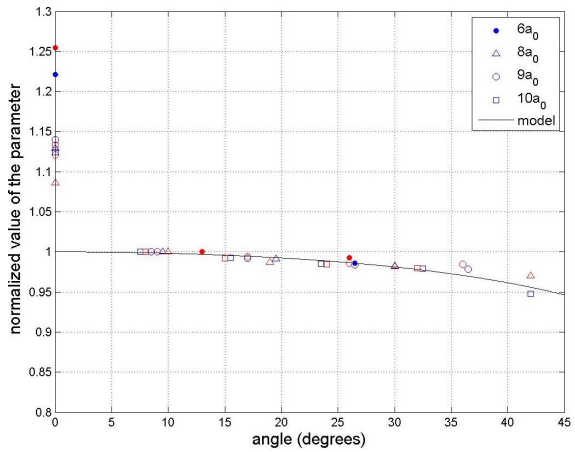


**Figure 4.9:** Direct transmission $t_0$ (= $p_1(\theta)$): angle dependence from the fits for two sets of data from repeated measurements (red and blue) for hole spacing $6a_0$, $8a_0$, $9a_0$ and $10a_0$. The model for the direct transmission from Yi and Ebbesen (Eq. 1.12) is plotted with the black line.

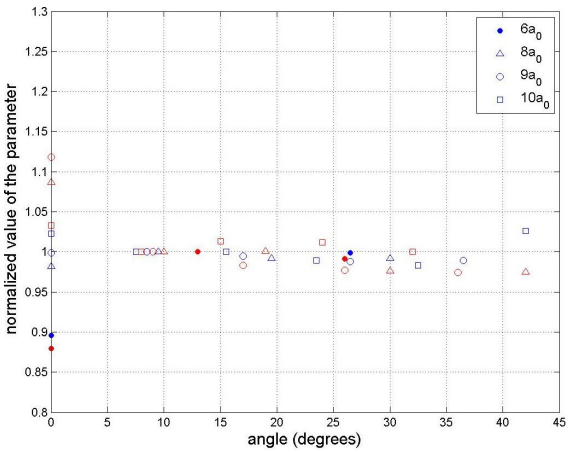


**Figure 4.10:** Resonant contribution $|\alpha\beta|$ (= $p_2(\theta)$): angle dependence from the fits for two sets of data from a repeated measurements (red and blue) for hole spacing $6a_0$, $8a_0$, $9a_0$ and $10a_0$.

The values of $p_1$ and $p_2$ in these figures lay on one line and both show the same angle dependence: the values vary by approximately 5% over 40°. So both the direct transmission and the resonant contribution seem approximately constant with angle. The comparison in Fig. 4.9 between the data and the model from Yi and Ebbesen (Eq. 1.12) shows that the model describes the angle dependence of the direct transmission very well. This model contains no fit parameters, it is just Eq. 1.12 with the dielectric constant of gold from [11]. Some of the highest diffraction orders could for some reason not be fitted well, so these points are not in the plotting range in the figures above. The errors on the fitting parameters are very small, so errorbars are not shown because they would be smaller than the datapoints.

## 4.3 Discussion

The spectra from Fig. 4.1 and Fig. 4.2 are different. We can see that the spectra for higher orders are cut off because of angular dispersion when using method A. Fig. 4.2 shows that all spectra are complete for method B. The effect of the incomplete spectra is not visible in Fig. 4.3 and Fig. 4.4 because we look at the intensity of only one wavelength in the diffraction orders.
Another difference between the spectra shown in Fig. 4.1 and Fig. 4.2 is the intensity of the peaks. Methods A gives about 10% lower transmission but we could not understand the reason.

Since the model doesn't fit perfectly to our data, Fig. 4.9 and Fig. 4.10 are only an indication of the angle dependence, but not a strong evidence of the two separate contributions to the transmission. However, the spectra of the different diffraction orders in Fig. 4.8 are quite similar to each other. This is also the case for the other arrays besides $10a_0$. Also the normalized fit parameters are almost on one line, which indicates a quite constant emission profile in angle for both the direct transmission and the resonant contribution.
Although the fits are not so well, we show in Fig. 4.9 that the values we found for the direct transmission are accurately described by the dipole model (Eq. 1.12) from Yi and Ebbesen.

# Chapter 5

# Experiments ss configuration

We also measured the transmission through different hole arrays with both polarizers in y-direction, so in the ss configuration. This means that the SPPs propagated mainly in the $1a_0$ direction on the sample.
Transmission spectra were obtained in the diffraction orders with method A and method B while illuminating the sample from the glass side. We normalized the intensities in the diffraction orders and analyzed the angle dependence the total transmission. To obtain information about the angle dependence of the direct transmission and the resonant contribution we fitted Eq. 2.2 to the spectra.

## 5.1 Results

Transmission spectra in the ss configuration were obtained for four different arrays with hole spacing $6a_0$, $8a_0$, $9a_0$ and $10a_0$, but the array with $10a_0$ was measured only with method B. In Fig. 5.1 and Fig. 5.2 we show transmission spectra for the array with spacing $9a_0$ and for clarity only the zeroth order and first four positive diffraction orders are displayed.

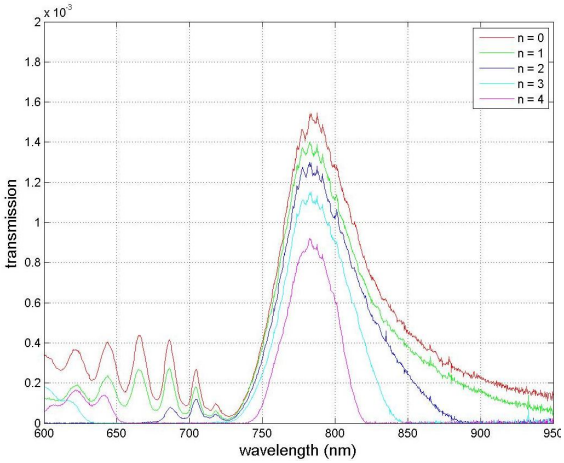


**Figure 5.1:** Transmission spectra for the diffraction orders of the array with spacing $9a_0$ obtained with method A in the ss configuration.

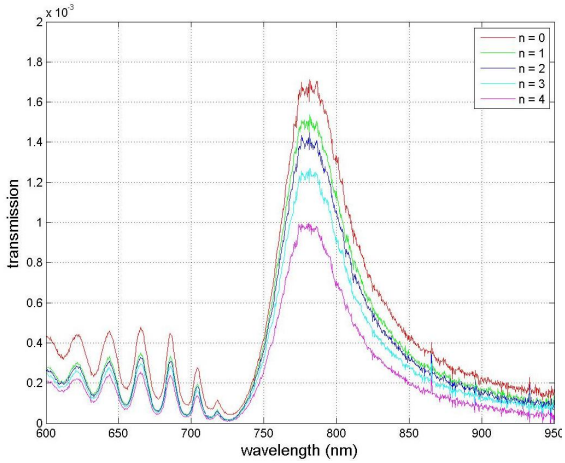


**Figure 5.2:** Transmission spectra for the diffraction orders of the array with spacing $9a_0$ obtained with method B in the ss configuration.

These spectra are different from those obtained in the pp configuration (if we compare Fig. 5.2 and Fig. 4.2). The resonance at 726 nm is still present, but since in the ss configuration the SPPs travel in $1a_0$ direction this is the only resonance in our wavelength range for all arrays. It will be visible in the spectra from all arrays and, as for pp measurements, for the analysis we will focus on the peak intensity value at 780 nm. Note that this peak wavelength of 780 nm in the ss configuration differs significantly from the peak wavelength of 748 nm in the pp configuration (see Fig. 4.1 and Fig. 4.2).
The resonances visible at wavelengths below 726 nm are present because SPPs do not propagate purely in one single direction but are excited in a narrow cone whose axis is along the direction of incident light polarization. This opens up the possibility for diagonal k-vectors to excite a resonance travelling also partially in the x direction. This requires bigger k values which explains why these additional resonances are at wavelengths shorter than 726 nm.

In the pp configuration all orders had approximately the same intensity (see Fig. 4.2), but in the ss configuration the transmission decreases for higher orders.
To visualize this decrease we looked at the intensities at 780 nm for spectra of the arrays with spacing $6a_0$, $8a_0$, $9a_0$ and $10a_0$. These intensities were normalized by dividing them by the intensity in the first diffraction order, because the zeroth order is too high. The results are plotted as a function of angle in Fig. 5.3 for method A and Fig. 5.4 for method B; in the latter, the accessible angle range is reduced by the amount of complete spectra which can be obtained.

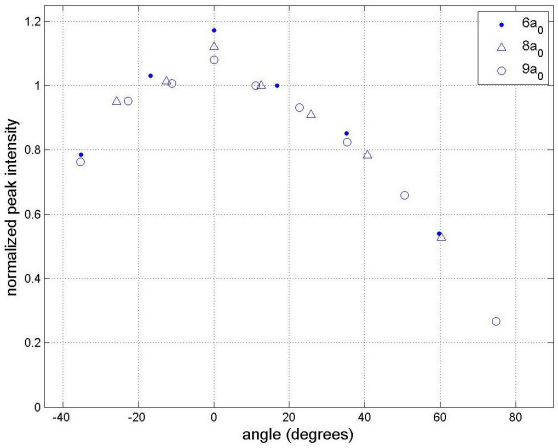


**Figure 5.3:** Normalized peak transmissions at 780 nm for $6a_0$, $8a_0$ and $9a_0$ obtained with method A.

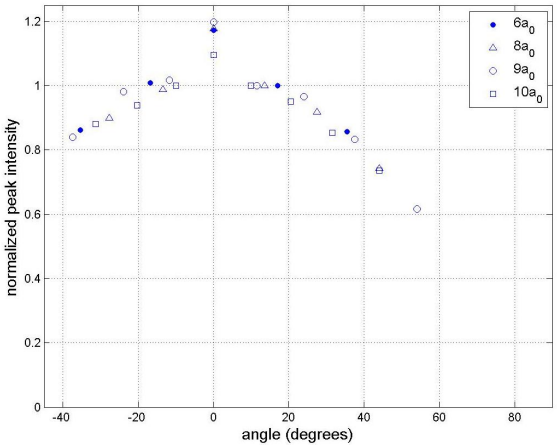


**Figure 5.4:** Normalized peak transmissions at 780 nm for $6a_0$, $8a_0$, $9a_0$ and $10a_0$ obtained with method B.

The normalized peak intensities for the ss configuration show a much stronger angle dependence than for the pp configuration in Fig. 4.3 and Fig. 4.4, where the variations are within 5% in the investigated angle range.

## 5.2 Analysis

It is possible to investigate the angle dependence in Fig. 5.4 with the model of electric and magnetic dipoles from Sec. 1.5. We fitted Eq. 1.11 to the data from Fig. 5.4 for all positive angles and these results are shown in Fig. 5.5.

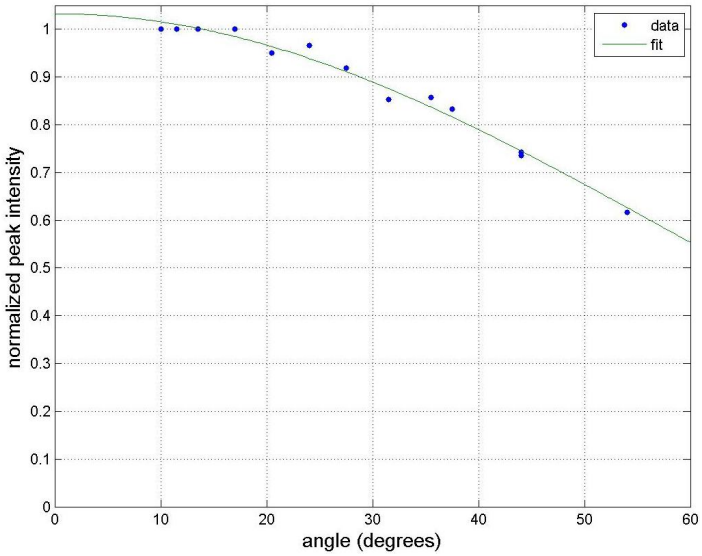


**Figure 5.5:** Data from Fig. 5.4 for positive angles with the fit of the dipole model (Eq. 1.11).

This gives $B = 0.4 \pm 3.5$ and $\phi = 0 \pm 203$ rad. With this value we can calculate the ratio of the fields of the electric and magnetic dipoles to be $\frac{E_m}{E_p} = 0.6 \pm 6.9$, but the error on this ratio is so large that it does not give us information, see Sec. 5.3.

In Fig. 5.5 we show the angle dependence of the total transmission, but we are also interested in the angle dependence of both the direct transmission and resonant contribution by SPPs. That information can be extracted by fitting Eq. 2.2 to the transmission spectra. The fitting is performed on the data obtained with method B because those are complete spectra, which is necessary for good fits. We fitted the zeroth order and positive diffraction orders for arrays with hole spacing $6a_0$, $8a_0$, $9a_0$ an $10a_0$. In the fitting procedure we fixed q = 1 for all arrays because in ss configuration the SPPs propagate mainly in the $1a_0$ direction. The spectra (blue and green lines) and fits (red lines) for the array with spacing $9a_0$ are shown in Fig. 5.6 in the wavelength range from 720 nm to 950 nm.

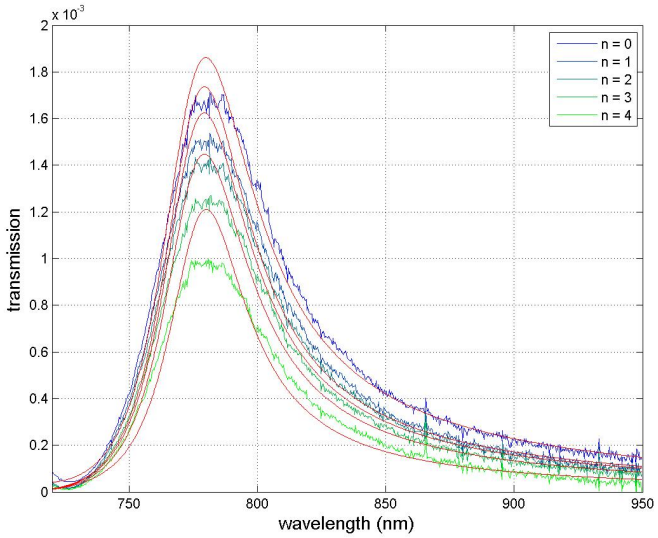


**Figure 5.6:** Transmission spectra (blue and green) and fits (red) of the array with spacing $9a_0$ for the zeroth order and positive diffraction orders.

Looking at the fits of our data we notice that the peak positions of the resonances are correctly fitted, but the fits overestimate the transmission in the peak region. This happens for all the diffraction orders in approximately the same way so we can still extract some information from them for the angle dependence. Just as in Sec. 4.2, five parameters are obtained from the fitting and we are interested in the direct transmission ($p_1$) and the resonant contribution by the SPPs ($p_2$). We normalize the parameters by dividing $p_1$ and $p_2$ in the diffraction orders of a certain array by the value in the first order of that array.
The fitting parameters for fits to the arrays with spacing $6a_0$, $8a_0$, $9a_0$ and $10a_0$ are plotted as a function of angle in Fig. 5.7 and Fig. 5.8.

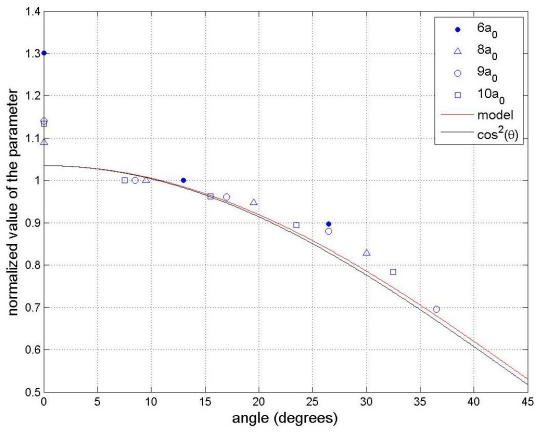


**Figure 5.7:** Direct transmission $t_0$ ($p_1(\theta)$): angle dependence from the fits for hole spacing $6a_0$, $8a_0$, $9a_0$ and $10a_0$ in the ss configuration. The model from Yi and Ebbesen (Eq. 1.12) for the direct transmission is plotted with a red line and a $cos^2(\theta)$ dependence is shown with a black line.

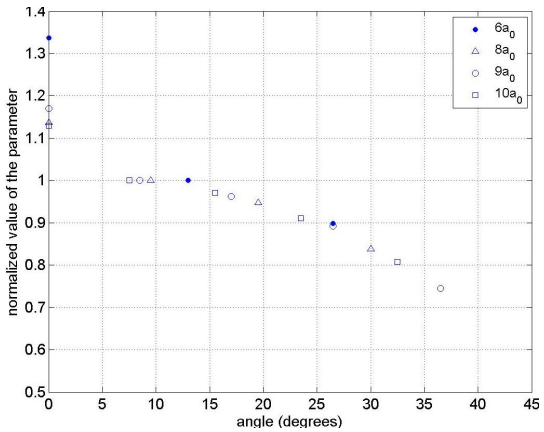


**Figure 5.8:** Resonant contribution $|\alpha\beta|$ ($p_2(\theta)$): angle dependence from the fits for hole spacing $6a_0$, $8a_0$, $9a_0$ and $10a_0$ in the ss configuration.

Although the values of $t_0$ and $|\alpha\beta|$ come from diffraction orders of four different samples, they draw one single angle dependence and both Fig. 5.7 and Fig. 5.8 show a similar trend. The errors on the fitting parameters are very small, so errorbars are not shown.
In Fig. 5.7 we show that both the model from Yi and Ebbesen for the angle dependence of the direct transmission and a $cos^2(\theta)$ dependence (which both contain no fit parameters) describe the angle dependence of our data very well.

Comparing Fig. 5.4 with Fig. 5.7 and Fig. 5.8 it is noticeable that $t_0$ decreases slightly faster with angle than $|\alpha\beta|$ and both decrease much faster than the total transmission. This is different because these two parameters are not the only two that describe the total transmission, but there are three more.
We stated that the total transmission can be described in terms of electric and magnetic dipoles and the interference between these can cause the intensity to be higher at larger angles. This interference is described by the combination of four parameters: $|\alpha\beta|$, $phase(\alpha\beta)$, $|\rho+\tau|$ and $phase(\rho+\tau)$, each with a certain angle dependence. The result of all contributions can thus have a different angle dependence than the separate contributions.

## 5.3 Discussion

Also in the ss configuration it is clear that in Fig. 5.1 a part of the spectrum is cut off for the higher orders due to angular dispersion, while Fig. 5.2 shows the complete spectra. But since we use only one wavelength (780 nm) for the analysis this is not a problem when looking at the angle dependence of the normalized peak intensities.
Just as for the pp configuration the spectra from method A have approximately a 10% lower intensity than those from method B and the zeroth order is higher than expected from the other orders (visible in Fig. 5.3 and Fig. 5.4).

Important is that the quasi cylindrical wave (QCW) plays a significant role in the ss configuration, since the distance between the holes ($1a_0$) is less than the damping length of the QCW. The QCW was found to increase the transmission with roughly factor 2 at $1a_0$ spacing [6]. This means that the fitting function we used (Eq. 2.2) is not suited for the spectra in this section. The supplementary information of [6] contains a function that includes the QCW contribution. This function is different from Eq. 1.7 only by a change in the $e^{ik_{SPP}qa_0}$ term, so it does not influence the angle dependence of $p_1$ and $p_2$ and Eq. 2.2 can be used to find that dependence.

Although the fits of Eq. 2.2 are not so good, we show in Fig. 5.7 that the values we found for the direct transmission are accurately described by both a $cos^2(\theta)$ model (Eq. 1.13) and the dipole model from Yi and Ebbesen (Eq. 1.12).

The figures in this section with the angle dependence of the total transmission or a fit parameter all show that also for the ss configuration the zeroth order is higher than expected from the other orders. In chapter 4 we explained this might be caused by the direct transmission through the gold film.

Fitting the dipole model to the total transmission in the ss configuration was problematic

(see Fig. 5.5 and the obtained values for $B$ and $\phi$). The transmission seems to follow a $cos(\theta)$ dependence and the best value for $\phi$ turns out to be very close to zero. As a consequence, the peak intensities calculated with the model don't depend on $\phi$ so the Jacobian (that we use to calculate the error) is close to zero and the inverse of the Jacobian (which is also used in the error calculation) becomes very large. This is the reason for the indefinite error on $\phi$ and this problem can be solved by fixing on of the free parameters in Eq. 1.11, namely by substituting $cos(\phi)$ by $cos(0) = 1$.

# Chapter 6

# Experiments with illumination on the chromium side

All data in the other sections were obtained with illumination on the glass side of the sample, but we also did series of measurements with illumination on the chromium side of the sample. In this section we show the results of those measurements.
Experiments with illumination on the chromium side were performed in both the pp configuration and the ss configuration for four different hole arrays. We used method B to obtain the spectra. Just as in chapter 4 and chapter 5 we looked at the angle dependence of the normalized intensity at a certain wavelength and fitted this with the model for electric and magnetic dipoles.

## 6.1 Results pp configuration

With the polarizers in pp configuration we scanned over the ($\lambda$,$\theta$) plane (method B) to obtain spectra in the diffraction orders for arrays with spacing $6a_0$, $8a_0$, $9a_0$ and $10a_0$.
In Fig. 6.1 we show the spectra for the array with $10a_0$ spacing in the zeroth order and five positive diffraction orders.

Just as for the pp configuration with illumination on the glass side we see Fano resonances in the spectra in Fig. 6.1. The positions of the resonances are approximately the same as in Fig. 4.2 and the common resonance at 726 nm is well visible in all the spectra.
The most striking differences with Fig. 4.2 are that the transmission in the diffraction orders is not constant and, moreover, the transmission of the fifth order in Fig. 6.1 is higher than that of the fourth order at a constant wavelength of 810 nm.

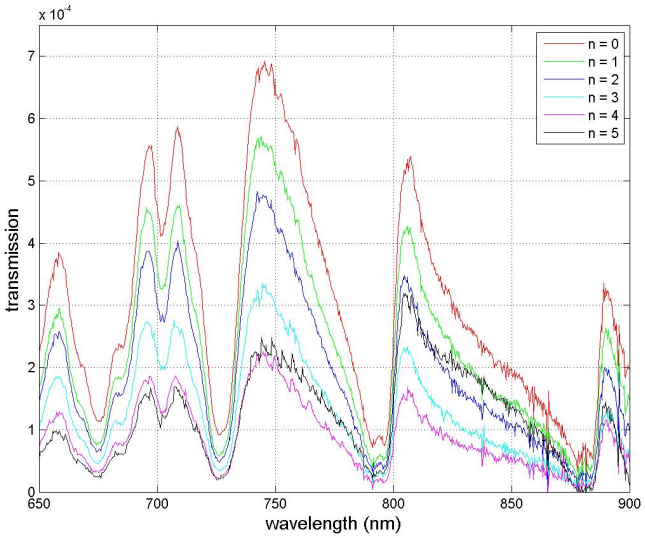


**Figure 6.1:** Transmission spectra for the diffraction orders of the array with spacing $10a_0$ in the pp configuration with illumination on the chromium side of the sample.

In Fig. 6.2 we show the dataset obtained with method B, it is visible how the intensity first decreases and then increases again for higher angles. This is clearer for shorter wavelengths which show more diffraction orders in the explored angle range. In Fig. 6.3 we show a section of Fig. 6.2 at 705 nm, which confirms that the intensity strongly increases at angles higher than 45°.

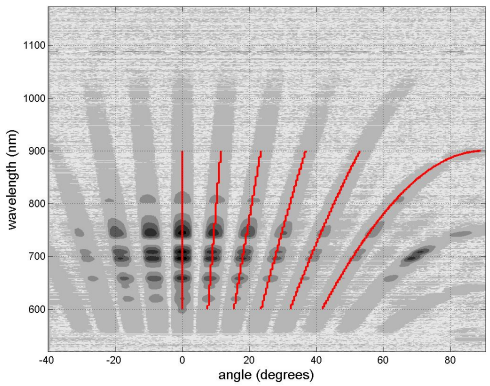


**Figure 6.2:** Intensity for the array with spacing $10a_0$ as a function of angle and wavelength from -40° to 90°. The red lines indicate the zeroth order and five diffraction orders.

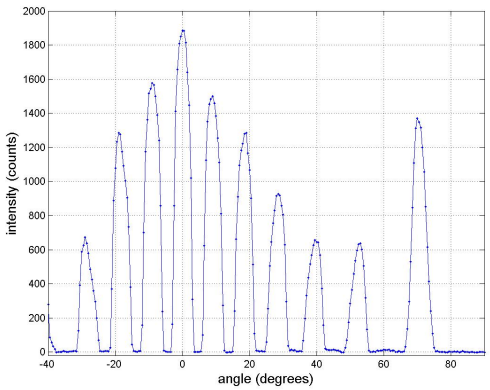


**Figure 6.3:** Section of Fig. 6.2 at 705 nm. It is also possible to see that the intensity between two diffraction orders is very close to zero.

To investigate the angle dependence of the total transmission for more arrays we look at the normalized intensities. In this case we used the intensities of the peaks around 705 nm, because in the 3D data set obtained with method B more orders could be extracted at that wavelength (this is visible in Fig. 6.2) so we could look at higher angles. The intensities were normalized by the first order intensity and the results are plotted in Fig. 6.4 for arrays with

spacing $6a_0$, $8a_0$, $9a_0$ and $10a_0$.

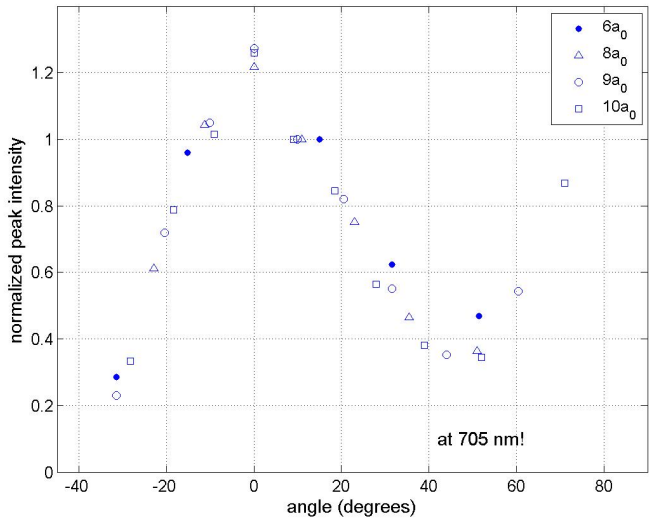


**Figure 6.4:** Normalized peak intensities of the total transmission at 705 nm for illumination on the chromium side with the polarizers in pp configuration.

From this plot an unexpected angle dependence emerges, very different from that in Fig. 4.4 for illumination on the glass side: the normalized intensity decreases faster showing a minimum around 45° before increasing again.

## 6.2 Analysis pp configuration

To analyze this angle dependence we fit the dipole model (Eq. 1.11) to Fig. 6.4. We exclude negative angles because of the asymmetry of our system and we exclude the zeroth order because it is too high compared to the other orders. The data and fit are shown in Fig. 6.5. This fit gives $B = 2.1 \pm 0.1$ and $\phi = 2.77 \pm 0.04$ rad. With this value we can calculate the ratio of the fields of the electric and magnetic dipoles to be $\frac{E_m}{E_p} = 0.69 \pm 0.02$, so the electric dipole radiation appears to be dominant from our data at 705 nm.

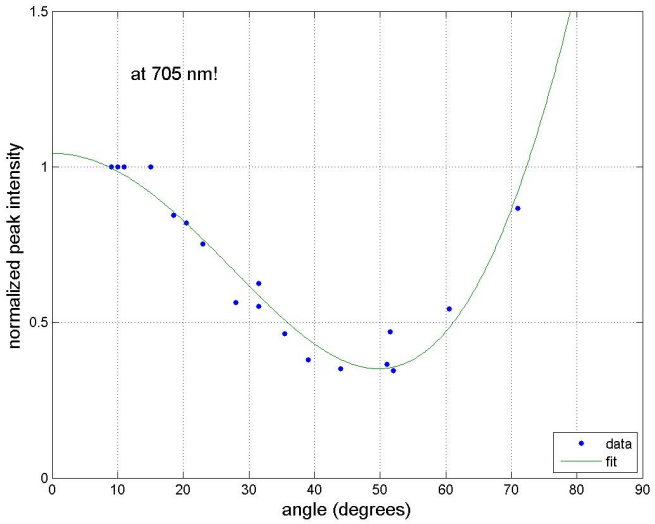


**Figure 6.5:** Fit of Eq. 1.11 for a combination of electric and magnetic dipoles to the data from Fig. 6.4 at positive angles

## 6.3 Results ss configuration

With the polarizers in ss configuration, we used method B to obtain spectra in the diffraction orders for arrays with spacing $6a_0$, $8a_0$, $9a_0$ and $10a_0$.
In Fig. 6.6 we show the spectra for the array with $10a_0$ spacing in the zeroth order and five positive diffraction orders.

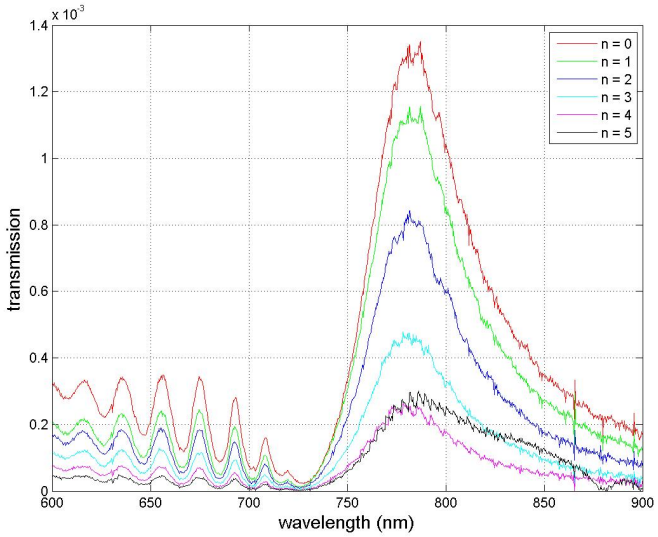


**Figure 6.6:** Transmission spectra of the $10a_0$ array for the zeroth order and positive diffraction orders in the ss configuration with illumination on the chromium side of the sample.

These spectra look quite similar to those in Fig. 5.2 for illumination on the glass side in the

ss configuration. The minimum of the common resonance is again at 726 nm and because the SPPs travel in $1a_0$ direction on the sample that is the only resonance in our wavelength range. As in Fig. 5.2 extra resonances are visible for wavelengths smaller than 726 nm because of the orthogonal component of the SPPs.
The transmission of the fifth order is for some wavelengths higher than the transmission of the fourth order, as we also observed in Fig. 6.1 for the pp configuration.

To investigate the angle dependence of the transmission we look at the normalized intensities. The intensities in the diffraction orders of the peak of the resonance (around 780 nm) were divided by the first order value to normalize them. The results for arrays with spacing $6a_0$, $8a_0$, $9a_0$ and $10a_0$ are plotted in Fig. 6.7.

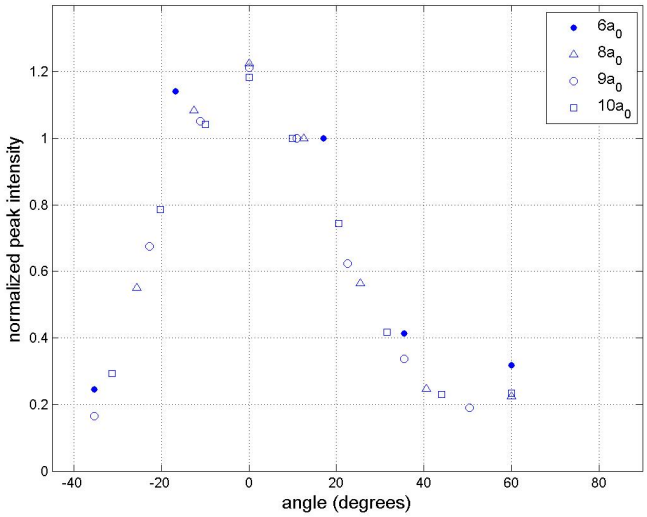


**Figure 6.7:** Angle dependence of the normalized peak intensities at 780 nm for illumination on the chromium side with the polarizers in ss configuration.

From this figure it is clear that there is a strong variation of the transmitted intensity with angle, different from that in Fig. 5.4 for illumination on the glass side. Fig. 6.7 looks similar to Fig. 6.4 for the pp configuration. Both show a rapidly decreasing normalized intensity with a minimum around 45° whereafter the intensity increases.

## 6.4 Analysis ss configuration

To analyze the angle dependence we fit the dipole model (Eq. 1.11) to Fig. 6.7, excluding negative angles and the zeroth order. The data and fit are shown in Fig. 6.8.

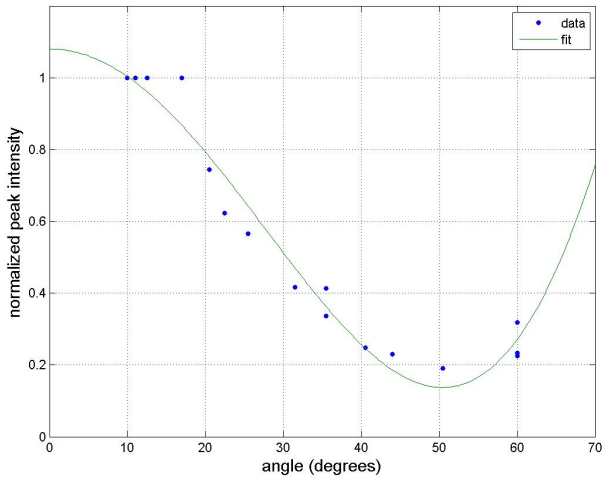


**Figure 6.8:** Fit of Eq. 1.11 for a combination of electric and magnetic dipoles to the data from Fig. 6.7 for positive angles.

This fit gives $B = 2.4 \pm 0.2$ and $\phi = 3.36 \pm 0.06$ rad. With this value we can calculate the ratio of the fields of the electric and magnetic dipoles to be $\frac{E_m}{E_p} = 1.53 \pm 0.02$, so the magnetic dipole radiation seems to be dominant in this case.

## 6.5 Discussion

All figures in this section show that illumination on the chromium side gives different results than illumination on the glass side. The results for ss and pp are more similar to each other than those for illumination on the glass side. Both Fig. 6.4 and Fig. 6.7 show a rapid decrease of the peak intensity with a minimum at approximately 45° . The depth of these minima is not the same in the two figures.
There is an asymmetry between positive and negative orders. For the negative angles the normalized peak intensity is 0.1 around 40° and for positive angles it is 0.15-0.3.

It is not yet clear why the angle dependence looks like this, but interference might be a factor since it plays an important role in our model (Eq. 1.11) which fits the angle dependence of the intensity quite well.
The ratio of the fields of magnetic and electric dipoles is $0.69 \pm 0.02$ for the pp configuration and $1.53 \pm 0.02$ for the ss configuration. These values are similar to those we found in experiments with illumination on the glass side. To compare the values we summarize the results in table 6.1. Although the error on the value for the ss configuration with illumination on the glass side is large, there seems to be a clear relation between the strength of the dipoles.

| experiment | Ratio fields dipoles |
|---|---|
| glass side: pp | 1.6 ± 0.3 |
| glass side: ss | 0.6 ± 6.9 |
| chromium side: pp | 0.69 ± 0.02 |
| chromium side: ss | 1.53 ± 0.02 |

**Table 6.1:** Summary of the ratio of the fields of the magnetic and electric dipoles for the experiments with illumination on the glass side and on the chromium side of the sample.

# Chapter 7

# Astronomical relevance

One of the main goals in astronomy is to obtain as much information as possible from electromagnetic radiation. To achieve this, constant research is needed to improve instruments for better measurements. Also knowledge of the radiative processes in space and a detailed understanding of light are crucial. The properties of light are studied in many different ways and there is a big overlap between physics and astronomy on these subjects.

This research project was performed at the physics department in the Quantum Optics group. But it is also a useful project from an astronomical perspective, because the processes, theory, optical elements and techniques that were used are also applied in astronomy.
The most obvious similarity between astronomical research and this project are the measurements of spectra, the data processing and working with polarization. Also all optical elements like polarizers, apertures, lenses, gratings and spectrometers are frequently used for both physical and astronomical purposes.

A large part of the theory applied to this project is relevant in astronomy: SPPs, dipoles, gratings and polarization.
SPPs are present on all metal-dielectric interfaces with discontinuities, so also on metal-coated reflection gratings that are used in astronomy. The Diffraction Grating Handbook [12] contains plots of the grating efficiency that show prominent peaks which are dependent of wavelength and polarization. These typical spectra are caused by SPP resonances and the theory of SPPs is used to predict where resonances will appear. Knowledge of these positions is required if the grating is used in for example a spectrograph. Otherwise a spectrum might be interpreted in the wrong way.

We used dipoles to describe in first approximation the transmission of light through the subwavelength holes, but there are more radiative processes that can be described in terms of dipoles. An example in astronomy is a dipole antenna consisting of two wires with a size smaller than the wavelength. The radiation pattern of such an antenna also has the shape of a horn torus (visible in Fig. 1.2) because of the oscillating current in the wires. A second example is the radiation of rotating neutron stars, which can be described in terms of magnetic dipoles.

Polarization is another subject in this project with an important astronomical relevance.

One application is research on exoplanets [13]: polarimetry (measuring the polarization of light) can be used to detect exoplanets.
A problem with detecting exoplanets is the large intensity difference between planet and star, so the planet is difficult to detect. Light emitted by a star can be considered unpolarized and becomes polarized by reflection off an exoplanet. Measuring the degree of polarization of the light thus increases the contrast between a star and a planet [14].
Polarimetry can also be used for investigation of the properties of exoplanets, since the polarization depends on for example the molecules in the atmosphere and the structure of the surface [14].

SPEX is an example of an instrument for high precision polarimetry for the characterization of planetary atmospheres [15]. It is designed for satellites that orbit planets in our solar system (Earth, Mars and Jupiter) and will characterize the properties of aerosol and cloud particles in planet atmospheres.

We worked with two polarization directions (s and p) in separate measurements. In astronomy this is not possible because atmospheric effects (like seeing) continuously distort the wavefront, causing a change in the image from successive measurements. This induces noise and spurious polarization signals [16]. A repetition of measurements is thus not always possible, but multiple measurements with different polarizations are required to deduce the degree of polarization. In the review paper by Snik and Keller [16] is described that spatial modulation is a way to do this. The incident beam is split up in two or more beams, which are filtered for different polarizations and detected. The results are combined to find the degree of polarization.

# Chapter 8

# Conclusions

In this thesis we presented a study of the polarization and angle dependence of the extraordinary transmission through a gold film with rectangular arrays of subwavelength holes. We wanted to learn more about the orientation and strength of the electric and magnetic dipoles which describe the transmission. To do this we studied the transmission in the diffraction orders of our sample for two different linear polarizations.
The angle dependence of the total transmission was analyzed by calculating the normalized peak intensities of the diffraction orders and fitting a model for interfering electric and magnetic dipoles to these data.
We also separated the direct transmission through the holes and the resonant contribution by SPPs by fitting a model from Liu and Lalanne [5] to the transmission spectra. The angle dependence of these two contributions were analyzed using two of the fit parameters.

The sample we used was already studied in the zeroth order in the past. We repeated those measurements and found different results: a higher transmission, redshifted peaks and broader resonances. Fits to the spectra gave a larger direct transmission $t_0$ and a larger $|\alpha\beta|$, so the coupling of light and SPPs is stronger, which both cause an increased transmission. We also found a smaller $|\rho + \tau|$, which corresponds to more losses and thus broader resonances. These are all evidences that the sample had changed: by analyzing the holes with SEM images we discovered that the holes look not circular anymore and that the hole diameter seems to be increased by about 10%.

We measured the EOT at higher diffraction orders of arrays with different hole spacing. With the polarizers in pp configuration the normalized intensity turned out to be approximately constant with angle and fitting with the dipole model gives: $\frac{E_m}{E_p} = 1.6 \pm 0.3$. Also the direct transmission and resonant contribution that we found were approximately constant with angle and the direct transmission matches neatly with the theory from Yi and Ebbesen. In the ss configuration the results are completely different. The angle dependence of the total transmission was not constant with angle and when fitting it with the dipole model we found the strange value of $\frac{E_m}{E_p} = 0.6 \pm 6.9$, giving no information about the dipole strengths. Also in this case the angle dependence of the direct transmission follows nicely the models from Yi and Ebbesen.

We also performed series of measurements with illumination from the chromium side. These

experiments show that the intensity of the total transmission has a minimum around 45° and increases for higher angles. This dependence was found for both the pp and the ss configuration. Fitting the transmission with the dipole model gives $\frac{E_m}{E_p} = 0.69 \pm 0.02$ for pp and $\frac{E_m}{E_p} = 1.53 \pm 0.02$ for ss.

With this research we showed that the used strategy can give information about the dipoles. Results from higher diffraction orders for arrays with different hole spacing can be put together, because the normalized intensities lay on one line. The direct transmission we measured matched with the theory and the simple model for interfering dipoles was able to fit the angle dependence of the total transmission in all experiments.
The limit of the research was in separating the direct transmission and resonant contribution, because the sample we used had changed so we did not know it's exact properties. To confirm our results these experiments should be repeated with a similar sample as we used from which we know all properties. For that goal a new sample will be produced.

# Bibliography


[1] H. A. Bethe, Theory of Diffraction by Small Holes, Phys. Rev., vol. 66, 163-182, October 1944.

[2] T. W. Ebbesen, Extraordinary optical transmission through sub-wavelength hole arrays, Nature, vol. 391, 667-669, 12 February 1998.

[3] R. H. Ritchie, Plasma Losses by Fast Electrons in Thin Films*, Phys. Rev., vol. 106, 874–881, June 1957.

[4] N. Rotenberg, Plasmon scattering from single subwavelength holes, PRL, vol. 108, 127402, March 2012.

[5] H. Liu and P. Lalanne, Microscopic theory of the extraordinary optical transmission, Nature, vol. 452, 728-731, April 2008.

[6] F. van Beijnum, Quasi-cylindrical wave contribution in experiments on extraordinary optical transmission, Nature, vol. 492, 411–414, December 2012.

[7] E. Hecht, Optics, 4th edition, Eddison Wesley, 2002, chapter 10.

[8] W. L. Barnes, Surface plasmon subwavelength optics, Nature, vol. 424, 824-830, August 2003.

[9] J. D. Jackson, Classical Electrodynamics, J. Wiley and sons, 1962, chapter 9.

[10] J. M. Yi and T. W. Ebbesen, Diffraction regimes of single holes, PRL, vol. 109, 023901, July 2012.

[11] P. Johnson and R. Christy, Optical constants of the noble metals, Phys. Rev. B, vol. 6, 4370–4379, December 1972.

[12] C. Palmer, Diffraction grating handbook, 6th edition, Newport Corporation, 2005, chapter 9.

[13] T. Karalidi, Flux and polarisation spectra of water clouds on exoplanets, Astronomy and Astrophysics, vol. 530, 1-14, 2011.

[14] C. Keller, Design of a polarimeter for extrasolar planetary systems characterization, Proc. SPIE, vol. 6269, 62690T, May 2006.

[15] F. Snik and C. Keller, SPEX: an in-orbit spectropolarimeter for planetary exploration, Proc. SPIE, vol. 7010, 701015, August 2008

[16] F. Snik and C. Keller, Astronomical Polarimetry: Polarized Views of Stars and Planets, Planets, Stars and Stellar Systems, vol. 2, 175-221, Springer 2013.